Chapter 8

Novel Experiments

8.1 Mechanical Stimulation

8.1.1 Motivation

Numerous reports suggest that the morphology of palladium (or its hydride) is critical to AHE. Mechanically working a metal sample can change its morphology. For instance, Violante used cold rolling to achieve the desired morphology [274]. He also supplied samples to Energetics [102]. Storms and Letts used a similar sample preparation involving cold rolling [104, 113]. Staker preconditioned samples by cyclic loading and deloading to obtain a fine-grained morphology [105]. Fundamentally, the morphology (strain fields, defect densities etc.) determines the energy landscape around hydrogen in interstitial octahedral sites as well as the hydrogen diffusion rates, which in turn could affect AHE.

In-situ mechanical deformation could drastically increase the number of states that are amenable to AHE present within a sample under investigation by continuously changing the energy landscape, creating defects and slipping atoms along each other. It would also create transient states that present potentially favorable configurations to AHE, that will otherwise have relaxed in the time period between ex-situ mechanical deformation and the experiment. To our knowledge, no in-situ mechanical stimulation experiments of palladium hydride during calorimetry have been reported in the literature.

In principle, all kinds of stress fields are possible: uniaxial tension, uniaxial compression, torsion, hydrostatic tension, hydrostatic compression. Hydrostatic compression is common during gas loading, which is outside of the scope of this study. Hydrostatic tension likely has the largest effect on the behavior of hydrogen in palladium hydride, but it is hard to achieve experimentally. Thus, uniaxial tension and torsion are of most interest and are easy to implement in practice. Specifically, in a wire under torsion, the highest strains are located near the sample surface, which is hypothesized to be the location of AHE. For this reason, torsion is the most attractive deformation mode.

8.1.2 Background

In unstrained palladium hydride, the hydrogen almost exlusively occupies the octahedral interstitial sites [189]. Tetrahedral sites are used only transitorily as hydrogen moves from one octahedral site to an adjacent octahedral site. Kimizuka and Akiba reported that in strained palladium hydride, the tetrahedral interstitial

sites become more favorable [275, 276]. This can increase the hydrogen diffusion rate by 20 times at room temperature [275]. Valiev reported that severe plastic deformation (SPD) can lead to non-equilibrium grain boundaries, deformation twins, dislocation substructures, vacancy agglomerates, and solute segregation and clustering. SPD-induced lattice defects can act as nucleation sites for hydrogenation [277]. Their stability is critical for the overall reproducibility of the absorption/desorption kinetics. Thus, hydrogen loading and deloading is much faster (or just as fast at a lower temperature) in SPD treated materials than in pristine materials. Hongo applied high-pressure torsion (HPT) to form an ultrafine-grained (UFG) structure with an average grain size of ~ 220 nm, resulting in increased hardness and tensile strength as well as increased plasticity [278]. This is in contrast to pristine palladium (with a grain size of tens of μm), which embrittles when loaded with hydrogen. The hydrogen-enhanced localized plasticity (HELP) is ascribed to hydrogen serving as solute atoms, increasing the dislocation mobility [279]. Dislocations which are generated during hydrogenation and dehydrogenation remain in the microstructure and enhance the hardness even after deloading [280, 281]. At an atomic level, the strain field around a dislocation effects an increase in hydrogen concentration within a radius of five to ten unit cells around the dislocation [279]. Increased diffusion rates and increased residence times of hydrogen ions in tetrahedral interstitial sites could present favorable conditions for AHE reactions.

8.1.3 Implementation

The mechanical properties of palladium hydride are shown in Fig. 8.1. For reasons listed above, we settled on a torsion geometry. The expected torsion angle at yield for a 0.5 mm diameter palladium wire is 14°, the torsion angle at break is 48°, and the torque at break is on the order of a few mNm. With increasing wire diameters, more torque is needed and the torsion angle at break will be reduced.

We defined the requirements for an in-situ mechanical deformation device during calorimetry as follows:

- The power transfer across the thermal boundary must be measured accurately. It might be easiest to measure electrical power and convert it to mechanical motion inside the boundary (as opposed to having a shaft crossing the thermal boundary).
- Torque or force must be enough to achieve yield on typical sample dimensions, ideally going beyond yield towards fracture.
- The strain rates must be high enough to perform cyclic experiments.
- Hydrogen loading must be measured at least prior to deformation, ideally also during deformation, using resistance measurements.
- Motor and gearing must be protected from corrosive electrolyte.
- The setup should fit into an HTcal vessel (section 2.7).

Our first design centered around a geared stepper motor (GM15BY-VSM1527-100-10D). However, with no eyes on the sample and long cyclic deformations applied to the sample, even occasional missed steps resulted in an indeterminate sample state. For that reason, an angle encoder (US Digital E4T-360-250-S-H-D-B, connected to a NI PXI-6608) was added and the stepper motor was replaced with a DC motor (Pololu Micro Metal Gear motor with 1000:1 gear ratio, #2373, run by a NI PXI-4141). The design of the mechanical stimulation cell that fits into an HTcal vessel is shown in Fig. 8.2.

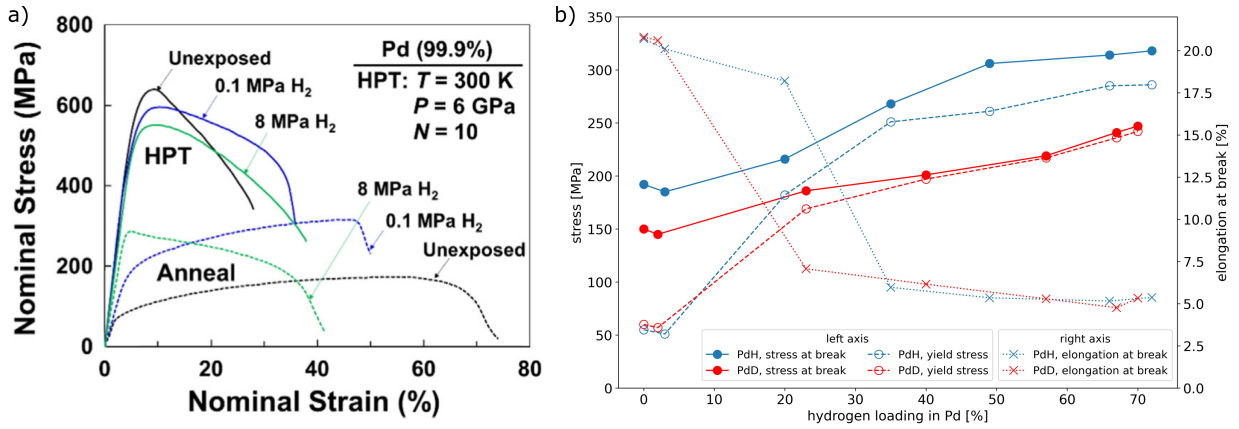

Fig. 8.1: Mechanical properties of palladium and palladium hydride. a) Stress-strain curves of palladium ("unexposed") and palladium hydride (with gas loading pressures as indicated). Source: [278]. b) Yield stress, stress at break and elongation at break as function of hydrogen loading. Composed with data from [282].

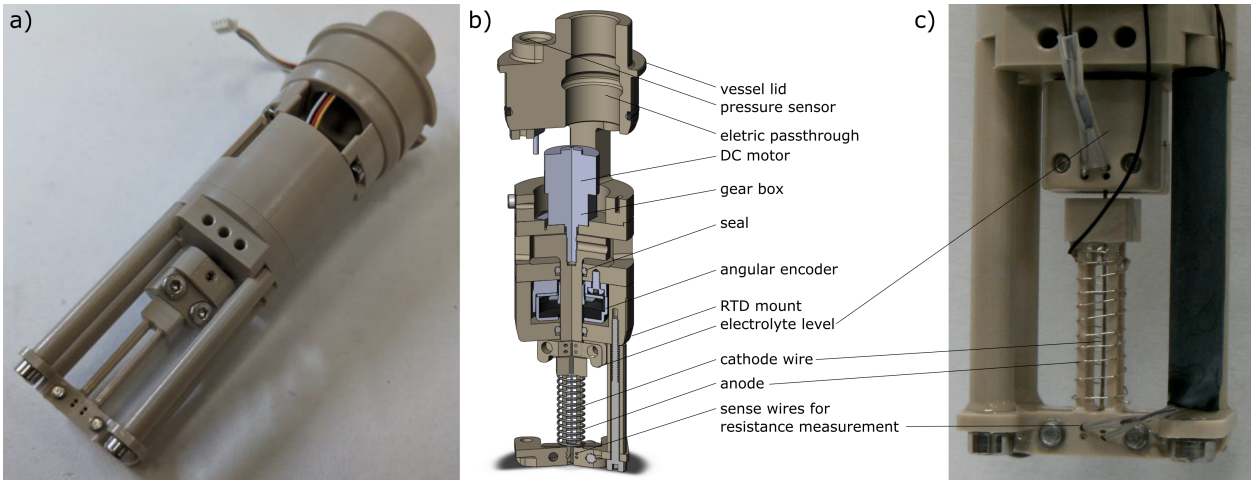

Fig. 8.2: Design of mechanical stimulation cell for in-situ deformation during calorimetry in HTcal. a) Photograph of mechanical stimulation cell during assembly. b) CAD rendering of mechanical stimulation cell with labeled components. c) Photograph of sample assembly with electrodes and four-wire resistance measurement.

8.1.4 Experiments and Results

Various mechanical deformation histories were applied to palladium and palladium hydride samples – before, during and after hydrogen loading. An example is illustrated in Fig. 8.3. Here, a 0.5 mm diameter palladium wire (99.9 %, Sigma Aldrich, surface treated with centerless grinding) is electrochemically loaded with deuterium in 0.5 M LiOD in D_2O at -55 mA for 9 h. During the 9 h electrochemical loading period, a combination of cyclic deformation and hold periods is applied (8.3 a). Every 95 cycles, a hold period of 5 minutes is applied and the torsional amplitude is increased. An overview of all calorimetry data channels is provided in Fig. 8.3 b. The magnitude of the excess heat is small compared to the input power, resulting in a COP close to unity. Similar results with no significant excess heat were obtained in all mechanical stimulation experiments.

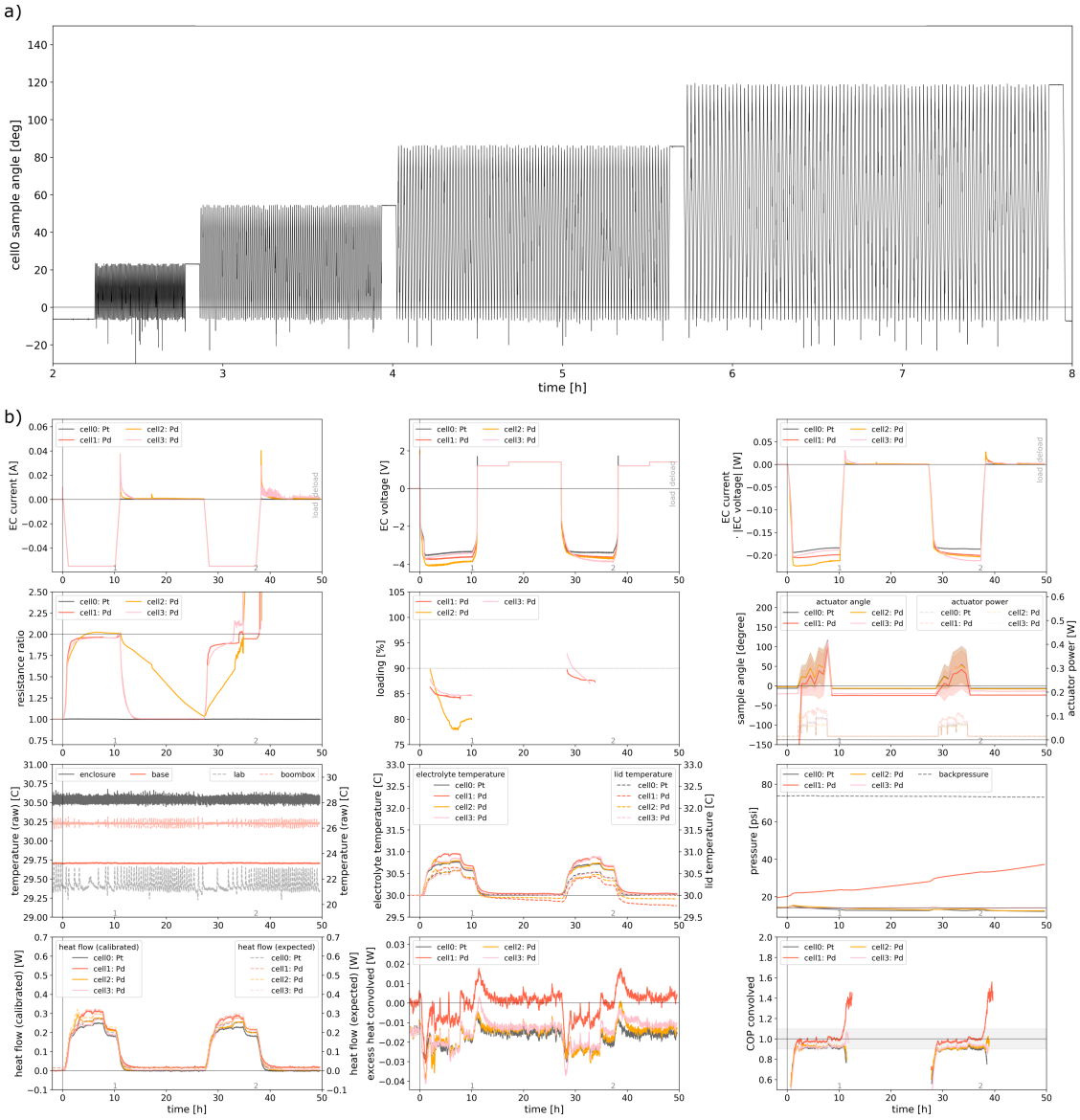

Fig. 8.3: Example of a mechanical stimulation calorimetry experiment in the HTcal with several hundred mechanical load cycles, mechanical load holds and two electrochemical load-deload cycles. a) Torsional deformation history applied to the sample during the nine-hour hydrogen loading period. b) Data channels of calorimetry experiments. The sample angle is resampled for better illustration. The actual sample deformation is indicated in a). The measured heat flow and the expected heat flow (from the total input power and the instrument response function) generally agree closely, resulting in a COP of unity. Cell 1 exhibits an elevated COP while the input power is being stepped down, indicating that the instrument response is not well modeled.

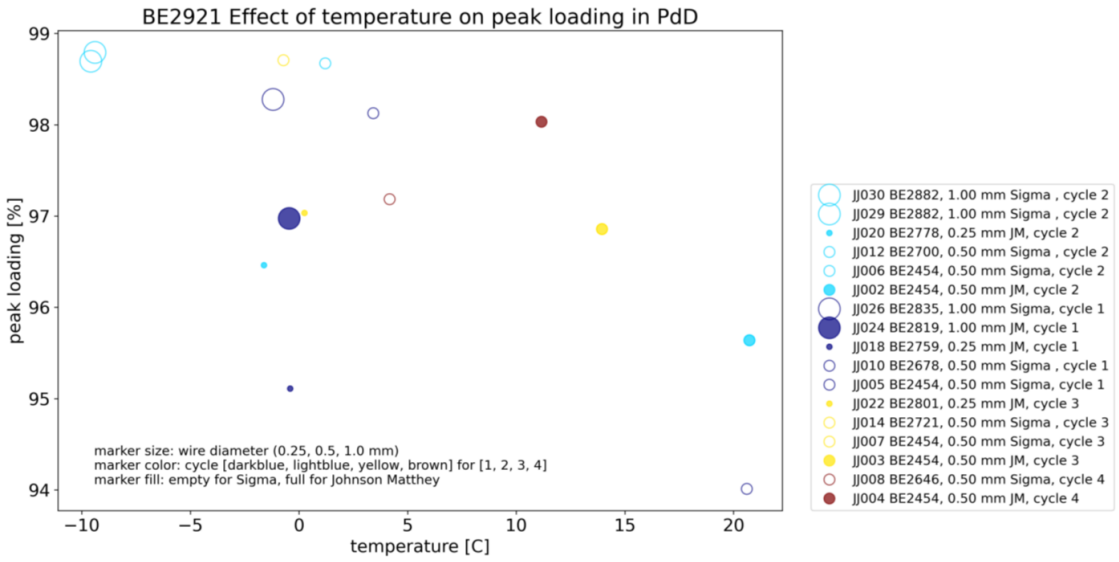

Fig. 8.4: Summary plot showing results of open cell loadings as a function of temperatures ranging from 20 to -10 °C.

8.2 Loading Enhancers

8.2.1 Loading Enhancers: Arsenic at Low Temperatures

From the results shown in Figure 6.2, it was clear that arsenic was the loading enhancer of choice. However, the loading enhancement achieved from the introduction of As was short lived and thus we began working on extending the longevity of the enhancement. We initially started with optimizing 'Coating X' further as we observed excess Pt content in the overlayer correlating with decreased peak loadings. This led us to studying As dosant in the previously mentioned membrane separator compartment. We then began to study the effect of lower temperatures on peak loading, as lower temperatures should slow the kinetics of HER during loading and 'Coating X' formation. Figure 8.4 shows the peak D loading values for loading experiments dosed with 25 mM $NaAsO_2$ dosant and carried out at temperatures between 20 and -10 °C. We observe a clear increase in loading enhancement as temperatures decrease though the mechanism of this enhancement is not clear. We believe it is related to a slowing of HER kinetics, specifically V-T, in conjunction with V-T pathway inhibition from 'Coating X' formation as stated earlier.

We needed to find an antifreeze additive to continue to explore this loading enhancement effect as a function of temperature below 0 °C. We screened ethylene glycol ($(CH_2OH)_2$), methanol (CH_3OH), and ammonia (NH_3) as additives to allow electrolysis at and below 0 °C without electrolyte freezing or ionic conductivity falling too low. Our studies showed excellent performance for loadings carried out below 0 °C in electrolytes containing ~20 % methanol, with multiple experiments showing above 98 % D loading for 15 hours. These studies clearly display the benefits of loading Pd at low temperatures in conjunction with As enhancement. Unfortunately, during electrolysis methanol generates CO_2 which accumulates in the headspace and leads to pressure build up. This was not a problem in open cell testing but would cause issues

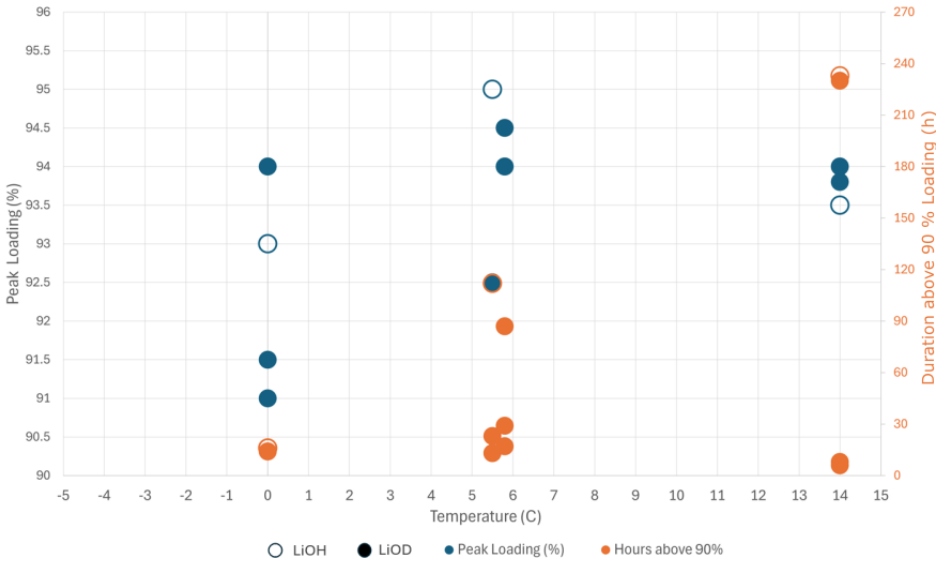

Fig. 8.5: Summary of the closed-cell, below room temperature loading studies with arsenic enhancement. Shown are the correlations between low temperatures (15 - 0 °C) and peak loadings (blue) and between low temperatures and loading longevity in this case, hours above 90% D/Pd (orange). Open circles indicate control cells in LiOH and closed cells represent LiOD.

in closed calorimetry testing.

As we investigated new additives, we found NH_3 to be a viable alternative to methanol as, while it could still produce unwanted gases in the headspace (i. e., $N_{2(g)}$, $H_{2(g)}$, and $NH_{3(g)}$), it could be used in much lower weight percentages in the electrolyte. In our control experiments using NH_3, we observed loading enhancement (~94 %) at room temperature without adding As enhancer and before lowering the temperature below 25 °C. This led us to the investigation of NH_3 as both a standalone loading enhancer and an additive to the electrolyte in conjunction with the As enhancer.

Continuing our investigation of loading enhancement with As below 25 °C, we moved our experiments to closed cell calorimeters as we've observed increased longevities (likely due to stabilization of electrolyte) in closed cells vs. open cells. In the open cell tests shown in Figure 8.4, an average time of loading enhancement was around 15 hours once the temperature set point was reached, with one outlier experiment being held for multiple days at D loadings ≥90 %. We developed an in-situ dosing strategy using syringe pumps and flexible polyethylene tubing lined with an inert fluoride coating tubing that allowed us to remotely introduce As enhancer into the system without opening the cells.

Figure 8.5 shows a summary of all of the closed-cell calorimetry experiments with peak loadings achieved and longevity of loadings ≥90 % as a function of average temperature. In these experiments we had not fully optimized anti-freeze additives to the electrolyte and subsequently avoided lowering temperature below 0 °C to avoid electrolyte freezing. Our open-cell results showed that the majority of our highest loadings occurred below 5 °C. As observed in the figure, we were able to achieve peak longevities for D loadings of ≥ 90 % for more than 230 h. We also achieved peak loadings of 95 % but did not see near 100 % loadings as

observed in open cell testing at -10 °C. We did observe some higher peak loadings as temperatures decreased, however freezing near 0 °C introduced major obstacles to closed cell As dosing and prevented long duration experiments.

8.2.2 Loading Enhancers: Ammonia Additives

Considering our previously observed loading enhancement at room temperature using NH_3 as an additive, we wanted to answer two major questions: 1) what is the mechanism by which NH_3 was enhancing loading and 2) what are the optimal conditions to achieve maximum loading enhancement using NH_3. We first tried to understand the loading enhancement and considered what was occurring in our system as we electrolyzed NH_3 containing electrolyte. A major question was if the electrolysis of NH_3 yielded a compound that acted as an additive to 'Coating X' or whether there was a surface effect that ultimately acted as a Tafel poison. The electrolysis reactions of NH_3 in alkaline media are:

$$\text{anode}: \quad NH_3 \rightarrow \frac{1}{2}N_2 + 3H^+ + 3e^- \tag{8.1}$$

$$\text{cathode}: \quad 3H^+ = 3e^- \rightarrow \frac{3}{2}H_2 \tag{8.2}$$

$$\text{overall}: \quad NH_3 \rightarrow \frac{1}{2}N_2 + \frac{3}{2}H_2 \tag{8.3}$$

In aqueous media, NH_3 partially dissociates into NH_4^+ and OH^-. The ratio of NH_3 to NH_4^+ depends on the pH. In alkaline media, most of the species are present in the form of NH_3, about 10,000 times more abundant than NH_4^+ at pH = 13.5 (0.5 M LiOH) [283, 284]. NH_3 can form complexes with Pd^{2+} and Pt^{2+} at positive bias [285]. It is possible that Pt^{2+} ions going into solution are complexed and no longer poison the working electrode surface, leading to higher loading [285]. Another plausible mechanism is through tetraamine palladium complexes ($Pd(NH3)_4X$) which are known to form strong bonds with OH^- [286]. This strong bonding can extract OH^- from the surface, pushing the Volmer reaction equilibrium to the right, increasing the amount of adsorbed H on the Pd surface. We also observe a deviation from a trend observed with As enhancement where loading enhancements increased with cycling. Deviation in NH_3 containing electrolyte is possibly because during the deload, some of the Pd (now positively biased) gets complexed with NH_3 [285]. Another possibility is during deload, oxidation of NH_3 on the Pd surface forms N_2. N_2 is known to form strong bonds with Pd [285], which could deactivate some of the active surface similar to H_2 bubbles adhering to the surface.

We then investigated various concentrations of NH_3 to find the optimum amount of additive possible to achieve loading enhancement while simultaneously preventing excessive pressure build up from NH_3 electrolysis. These experiments are shown in Figure 8.6 where loadings are shown for multiple concentrations ranging from 5 to 28 % NH_3 in 0.5 M LiOH. From the plot it is clear that there was a negligible difference in peak loadings achieved between the lowest concentration (5 % NH_3) and the highest (28 % NH_3). Subsequently we carried out all of our resulting experiments out at this lower concentration to keep gases produced from electrolysis to a minimum.

8.2.3 Loading Enhancers: Arsenic with Single Crystal Palladium

One parameter that we adjusted in our experiments was the form factor of our Pd cathodes. We know that changing the form factor can impact loading and deloading as there is more (or less) Pd that can be loaded

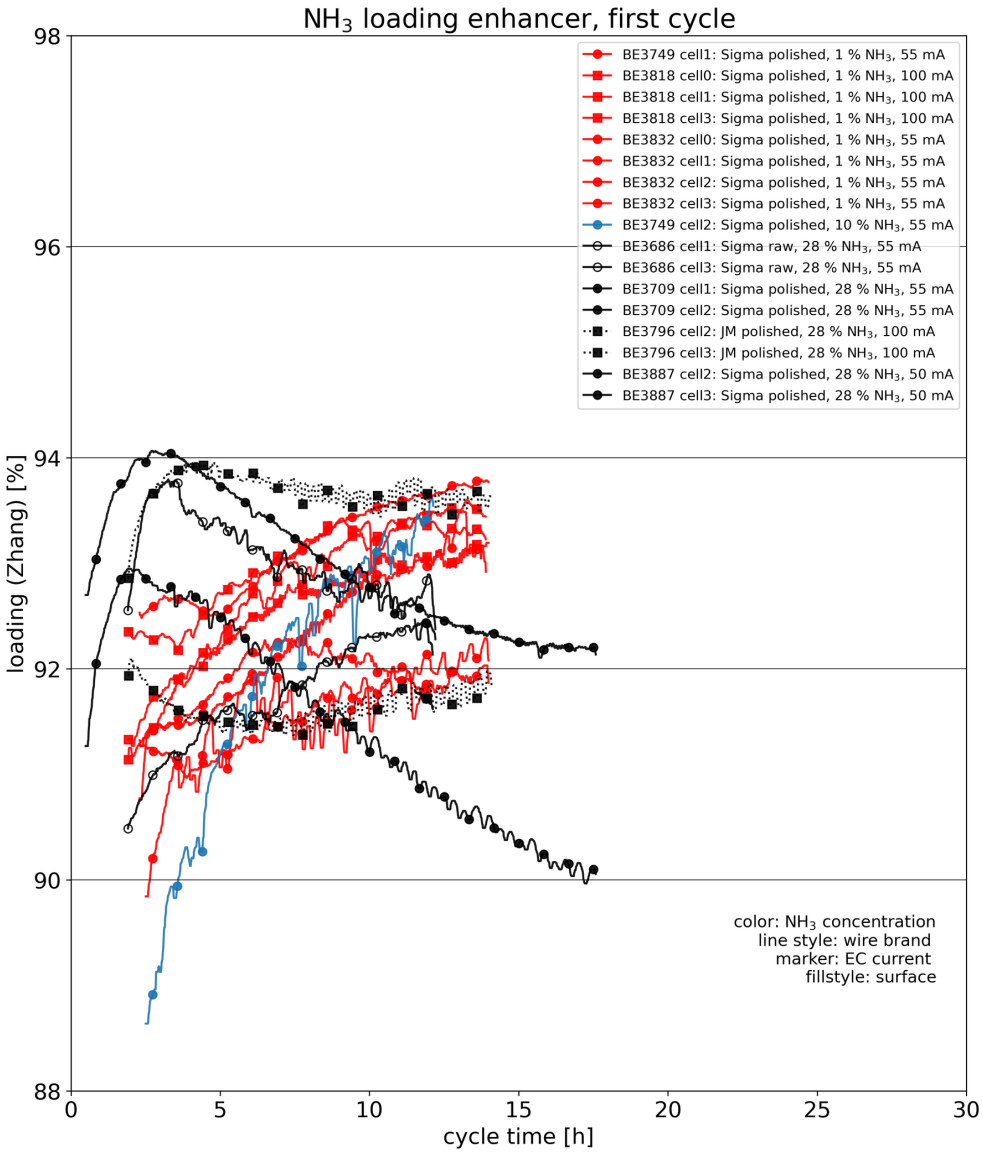

Fig. 8.6: Effect of NH_3 concentrations in 0.5 M LiOH electrolyte, EC current and wire preparation on hydrogen loading in palladium. The 0.5 mm diameter and 30 mm long Pd samples also had varying wire manufacturers (Johnson-Matthey, Goodfellow, and Sigma-Aldrich) with different processing (as-received or polished).

a)

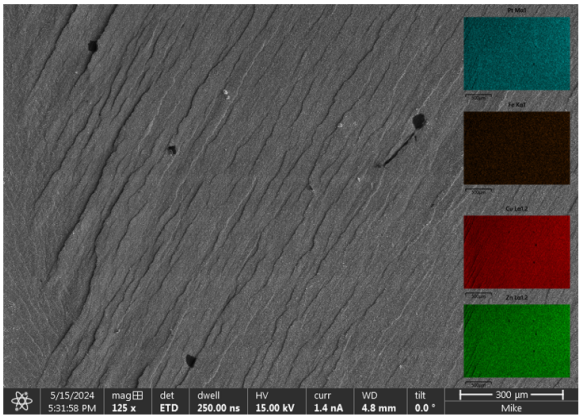

b)

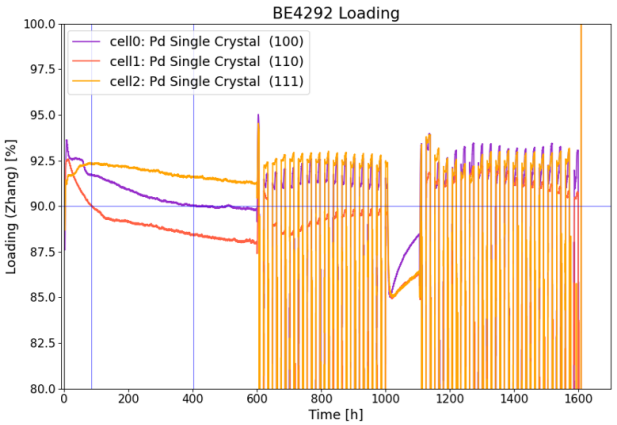

c)

Sample (in LiOD)	Cycle 1 (h) (BE4261)	Cycle 2 (h) (BE4261)		Cycle 3 (h) (BE4292)		Cumulative Time (h) >90% D/Pd
	Dose 1	Dose 1	Dose 2	Dose 1	Dose 2	
Cell 0 (100)	0	370	189	401	900	1860
Cell 1 (110)	10	144	59	83	494	780
Cell 2 (111)	0	0	237	600	870	1707

Fig. 8.7: a) Representative SEM with EDS false color map of sample surface post mortem. (No As represented on surface, though it was present in various areas on the samples.) b) Results from a long duration single crystal experiment with both DC and AC stimulation applied to all three (100), (110), and (111) orientations. The system was dosed with 25 mM $NaAsO_2$ three times, once at the start of long duration constant current application (~1 hour), followed by a dose at the start of each AC stimulation application (~600 and ~1100 hours). The horizontal line depicts the 90 % D/Pd loading threshold. c) Table summarizing the cumulative time above the 90 % D/Pd loading threshold for the total experimental time for the samples, spanning two experimental campaigns (BE4261 and BE4292).

and currents have to be adjusted to accommodate that change. Additionally, it has been established that differences in the crystal orientation of exposed facets in Pd cathodes exhibit different hydrogen absorption and desorption mechanisms, and by extension have a direct impact on loading [287]. Johnson et al. monitored the α- to β-phase transition in Pd (100), (111), and mixed (100) and (111) nanocrystals using in-situ X-ray diffraction (XRD) to indicate rate of H adsorption and desorption. This α- to β-phase transition in the Pd crystal structure is indicated by a shift in 2θ peak position in the XRD diffractogram. The rate of this transition can directly correlate the amount of H entering and exiting the Pd lattice. They discovered that the initial H uptake and release was much quicker for the mixed Pd and Pd (100) nanocrystals, with the transition from β- to α-phase (deloading) being an order of magnitude slower for the Pd (111) nanocrystal compared to other samples. Of course, this sluggish β- to α-phase transition observed in the Pd (111) orientation translates to a slower deloading process once loaded and ultimately highlights a difference in crystal orientation regarding H loading that could be leveraged for AHE.

To investigate further, we set up a series of experiments observing the effect of different Pd single crystal

orientations ((100), (110), (111)) on loading with As loading enhancement. The results of these studies are shown in Figure 8.7. The figure shows post-mortem SEM/EDS sample analysis showing the presence of Coating X elements on the surface (As is absent from the coating despite dosing, likely due to the long duration of the experiment), loading analysis for the final 1600 h of the experiment for each (100), (110), and (111) Pd orientation, and a summary plot of time of D loading ≥90 % for each orientation resulting from As enhancement doses. While the representative data shows our champion results from long-duration AC stimulation current on Pd single crystal samples (well over two months above ≥90 % loading), multiple DC stimulation studies were also carried out. Our studies aligned with the hypothesis we formed from Johnson et al. where we expected Pd (111) to stay loaded longer than the (110) and (100) orientations due to slower deloading kinetics. Interestingly, we found that the Pd (110) orientation tended to load lower and fall below 90 % D loading quicker than the Pd (100) and (111) upon the first cycle. As stated earlier, we have observed a positive correlation between peak loadings, loading longevities, and cycling (with diminishing returns after the fourth cycle on average). Studies show that with cycling, Pd (111) begins to outperform the Pd (110) and (100) orientations regarding peak loadings and longevities. This behavior could not be explained by postmortem SEM/EDS analysis, as all the Coating X constituents and coating characteristics were similar between orientations. Our hypothesis is that the orientation is initially less favorable to Coating X formation but as cycling progresses the coating is allowed to build up and inhibit D loss. It would appear an opposite effect would be at play for the Pd (110) orientation which exhibited lessened peak loadings and longevities as a function of loading. This change in loading longevity and by extension, lessened V-T inhibition is still being investigated. It is also likely that these differences between orientations could be sample dependent as we carried out multiple single crystal studies, but this was our flagship long-duration test lasting >400 hours.

8.3 Single Crystals

8.3.1 Introduction

The vast majority of studies in the LENR literature focus on a host palladium (Pd) lattice, which is an exemplary metal for its ability to intake large amounts of hydrogen isotopes with relatively little driving force. The original Fleischmann and Pons studies focused on using polycrystalline Pd [240, 288, 289]. These early studies looked at relatively large samples, with the rods ranging in diameter 1 mm to 20 mm, or in terms of mass between 100 mg and 60 g. The samples were typically sourced from Johnson Matthey and were claimed to be of very high purity (>99.9%$_{at}$). Subsequent work by the community in the 1990s and 2000s continued to focus on polycrystalline palladium, with minimal exploration of other alloys and formfactors. Notably, some people including Edmund Storms looked at Pd-Ag alloys [290]. Groups like SPAWAR explored nanostructured palladium [266]. More recently, the LENR community has explored metals beyond Pd, with one of the major motivations being the prohibitive cost of palladium. Researchers have looked at nickel (Ni) as a possible nuclear active material [291, 292]. One of the critical questions that has plagued researchers throughout the LENR field has been, "Why palladium?" What is special about this material that allows for the production of excess heat? There are certainly characteristics that make it stand out among metal hydrides. These include a relatively low temperature for absorption and desorption of hydrogen isotopes, a relatively high volumetric storage density, and its exceptional hydrogen solubility. Palladium can absorb hydrogen at concentrations approaching a hydrogen-to-palladium ratio of 1:1 (if sufficient gas pressure or electrochemical driving force is applied), much higher than most other metals at standard pressure and near room temperature. Of course, there is no fundamental mapping of these characteristics to the generation

of excess heat, but they are certainly interesting to note. In our own effort, we aimed to test out different purities, form factors, and compositions in order to try and deterministically understand how the material characteristics of a metal hydride influence the ability to generate excess heat. Admittedly, after exploring many different alloy compositions, form factors, sample masses, crystallinities, etc., we never arrived at excess heat. Despite this, the next section will highlight some of the major experimental efforts that we pursued, notably our efforts with single crystals and various alloy compositions.

Solid metals are inherently crystalline, meaning they have a well-defined, periodic atomic structure. However, over extended length scales, defects can occur, disrupting this symmetry. These include point defects, dislocations, and grain boundaries. Interestingly, these defects can be kinetically favorable, so most metals exist in a polycrystalline form. The material's morphology includes characteristics such as grain size (small or large), grain shape (elongated or equiaxed), grain boundary angles (high or low), and surface roughness (which can be influenced by dislocations). Due to variations in sourcing, manufacturing, and post-treatment processes, the morphology of palladium can vary significantly. Palladium from the same vendor and with the same form factor and composition may exhibit similar morphologies, while material from a different vendor, despite having the same nominal composition and form, may have nuanced morphological differences. Changes in the ore source over time can also affect impurity concentrations. For example, in the 1980s the primary source of palladium ore was the Norilsk-Talnakh mining complex in Russia, with modest contributions from South Africa's Bushveld Igneous Complex [293]. Today, although Russia and South African deposits remain significant portions of the market, the Sudbury Basin in Canada and Zimplats mine in Zimbabwe are becoming prominent suppliers. As a result of the change in ore supply and nuanced differences in purification and manufacturing, one of the major challenges facing the LENR community has been understanding why certain palladium samples allegedly exhibited nuclear activity while others did not.

8.3.2 Experiments

Figure 8.8a shows an x-ray diffraction pattern of nominally similar palladium from four different manufacturers. The differences in diffraction patterns reveal that there are different grain sizes for each of these manufacturers. These grain sizes are correlated with loading performance which is shown in Figure 8.8b. We found that smaller grains gave higher deuterium electrochemical loadings, when all other parameters were controlled. Assuming the observed instances of excess heat are not simply false positives (which is plausible and currently the conclusion of our team's work), we must ask how we can map these material characteristics to any observed excess heat deterministically. We decided that using single crystal palladium samples would provide the best chance for this determinism. Unlike polycrystalline palladium, single crystal palladium maintains pristine lattice symmetry across its entire macroscopic dimension, with few to no point defects, dislocations, or grain boundaries. This not only provided a blank canvas for monitoring changes to the morphology directly resulting from our experiments, but also allowed us to know with high confidence, the exact nature of our material. However, growing single crystal materials is challenging. When we decided to pursue single crystal palladium, there were no commercial suppliers available. We commissioned Princeton Scientific, experts in single crystal materials, to begin growing single crystal palladium for us. Initially, we obtained small ingots approximately 8 mm in diameter and 25 mm in length. We specified three surface terminations corresponding to the primary crystallographic planes in face-centered cubic materials: (100), (110), and (111), as shown in Figure 8.9. As Princeton Scientific improved their growth techniques, we were able to source larger samples.

The ultimate goal was to machine single crystal bars with a high aspect ratio for electrical resistance studies. The high aspect ratio would allow us to make accurate resistance measurements and better under-

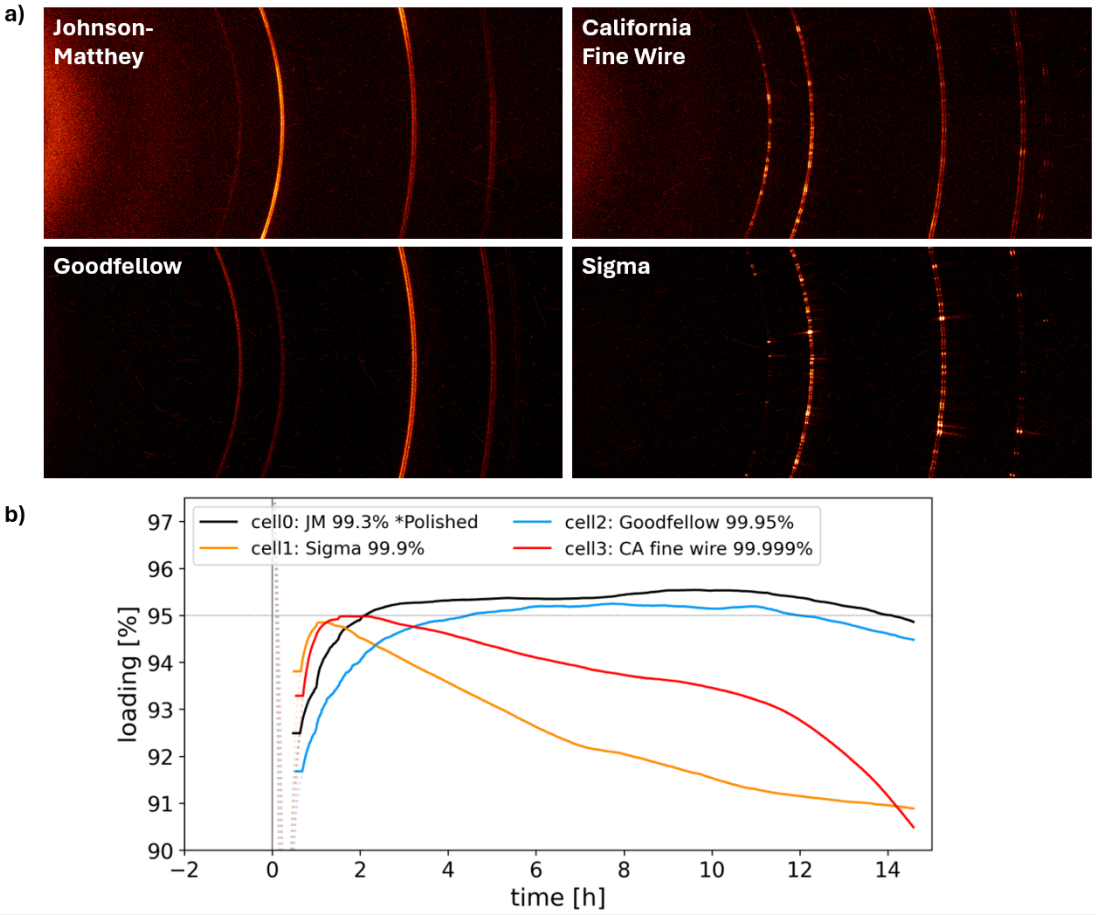

Fig. 8.8: a) X-ray diffraction (XRD) pattern of as-received Pd samples from four different manufacturers (Johnson-Matthey (polished), California Fine Wire, Goodfellow, and Sigma-Aldrich). The peaks in the XRDs are (from left to right) 111, 002, 022, and 222. b) Is a comparison of deuterium loading performance of each wire manufacturer as a function of time when exposed to similar loading conditions (i.e., 0.5 M LiOH, -50 mA of current, and 2 mL of 25 mM $NaAsO_2$).

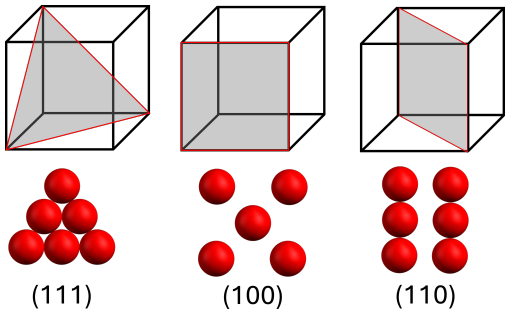

Fig. 8.9: 3D representation made in house of surface terminations corresponding to the primary crystallographic planes in face-centered cubic materials: (111), (100), and (110).

stand the effect of crystal orientation on loading capacity and kinetics. Ultimately, we went through four generations of sample sizes. The first generation consisted of 10 mm diameter disks with a thickness of around 500 μm. The second generation featured small bars, 4 mm x 8 mm x 500 μm, cut from the center of the ingots. The third generation involved medium-sized bars, 3 mm wide and 12-15 mm long, requiring more advanced machining techniques. For these, we cut ingots with different orientations, such as a (111) ingot, at off angles to expose the (100) surface. X-ray diffraction was used to orient the samples before machining to ensure accuracy. In the final generation, we achieved high aspect ratio single crystal bars with dimensions of 3 mm x 30 mm x 500 μm by contracting Princeton Scientific to grow 50 mm diameter single crystal wafers, from which the bars were cut using electrical discharge machining. All generations were polished to <5 nm roughness through a combination of mechanical polishing and ion milling. The final generation of samples was likely the largest diameter single crystal palladium ever produced –a notable achievement for our materials research efforts, even if not broadly significant. Due to the precious nature of these single crystal samples, we were more selective in deploying them for calorimetry studies. In total, we performed 35 studies, which are briefly described below. It is important to note that although the use of these samples would have allowed for deterministic understanding, the lack of excess heat precluded this type of understanding.

8.3.3 Overview of Experimental Results

We characterized the crystal structure of the prepared samples using x-ray diffraction (XRD). The diffraction patterns revealed excellent monocrystallinity, particularly in contrast to polycrystalline samples, which showed distinct patterns. This quality check was especially important for the medium-sized samples, which were obtained through off-angle cuts. Miscalculations or poor cutting could have compromised monocrystallinity, but we consistently produced high-quality monocrystalline surfaces across all sample generations. Nearly a dozen experiments comprised the initial calorimetry tests on single crystal samples, conducted using the MS80 differential calorimeter (section 2.8.1), which offered excellent sensitivity. However, as the number of tests increased, the calorimeter became difficult to operate, and we eventually replaced it with the HTCal model. These experiments explored high-frequency electrochemical stimulation and the use of arsenic salts to enhance deuterium loading. No definitive excess heat was detected, with false signals attributed to transient recombination events and electrical interference due to corroded contacts, which were easily explained. It

should be noted that there was a COP ~1.05 in one experiment (BE1320) that was never explained, however the test conditions were repeated, and the result was never reproduced. There was not sufficient confidence in this one-time result to attribute it to a nuclear origin. Several experiments (BE1724, BE1785, BE1779, and BE2071) mirrored the previous set but were conducted using the HTCal system. Although HTCal had a higher detection threshold than the MS80, its increased throughput allowed us to test twice as many single crystals at one time. High-frequency electrochemical currents were again applied to perturb the electric field at the surface, but no excess heat was observed. The most prominent false signals were due to transient recombination. With the development of large aspect ratio single crystal bars, we expanded our testing conditions using the HTCal calorimeter. These experiments applied high DC current densities to optimize deuterium loading without the need for arsenic enhancement. No excess heat was observed, and again the primary false signals came from transient recombination events. Additional large aspect ratio experiments aimed to induce excess heat by applying high-frequency perturbations to the electric field at the surface of palladium deuteride single crystals were carried out. We focused on frequencies between 10 mHz and 10 Hz, where we expected the greatest impact on the structure of the electric double layer. This is due to both experimental availability and because of the inverse relationship between frequency and measured capacitance of the the electronic double layer. The ability of the double layer interface to store charge at high frequencies is reduced because only ions near the electrode surface have enough time to respond to the rapidly changing potential [294]. No excess heat was observed during these tests.

8.3.4 Overview of Single Crystal Morphology Changes from Electrochemical Loading and Stimulation

Electrochemical testing led to significant changes in sample structure and surface composition of palladium single crystals. Deuterium cycling resulted in a loss of monocrystallinity, increased surface roughness, and substantial distortion of the form factor. Figure 8.10a illustrates the transition from point-diffraction to ring-diffraction patterns, as well as the broadening of peaks, indicating the introduction of grain boundaries, point defects, and line defects. Cycled foil samples often became twisted and crumpled, with large volumetric changes due to the stresses developed during deuterium charging and discharging. This is shown in Figure 8.10b. These changes, more significant than those typically reported in the literature, are likely due to the starting single crystal state, where the introduction of defects caused more pronounced macroscopic distortions. Additionally, Coating X (see section 6.3) was observed on most samples, regardless of whether DC or AC conditions were applied. The composition of Coating X varied depending on the reaction vessel used, with Pt, Cu, Fe, Sn, and Pb often present. These morphological changes were noted in both hydrogen and deuterium isotopes.

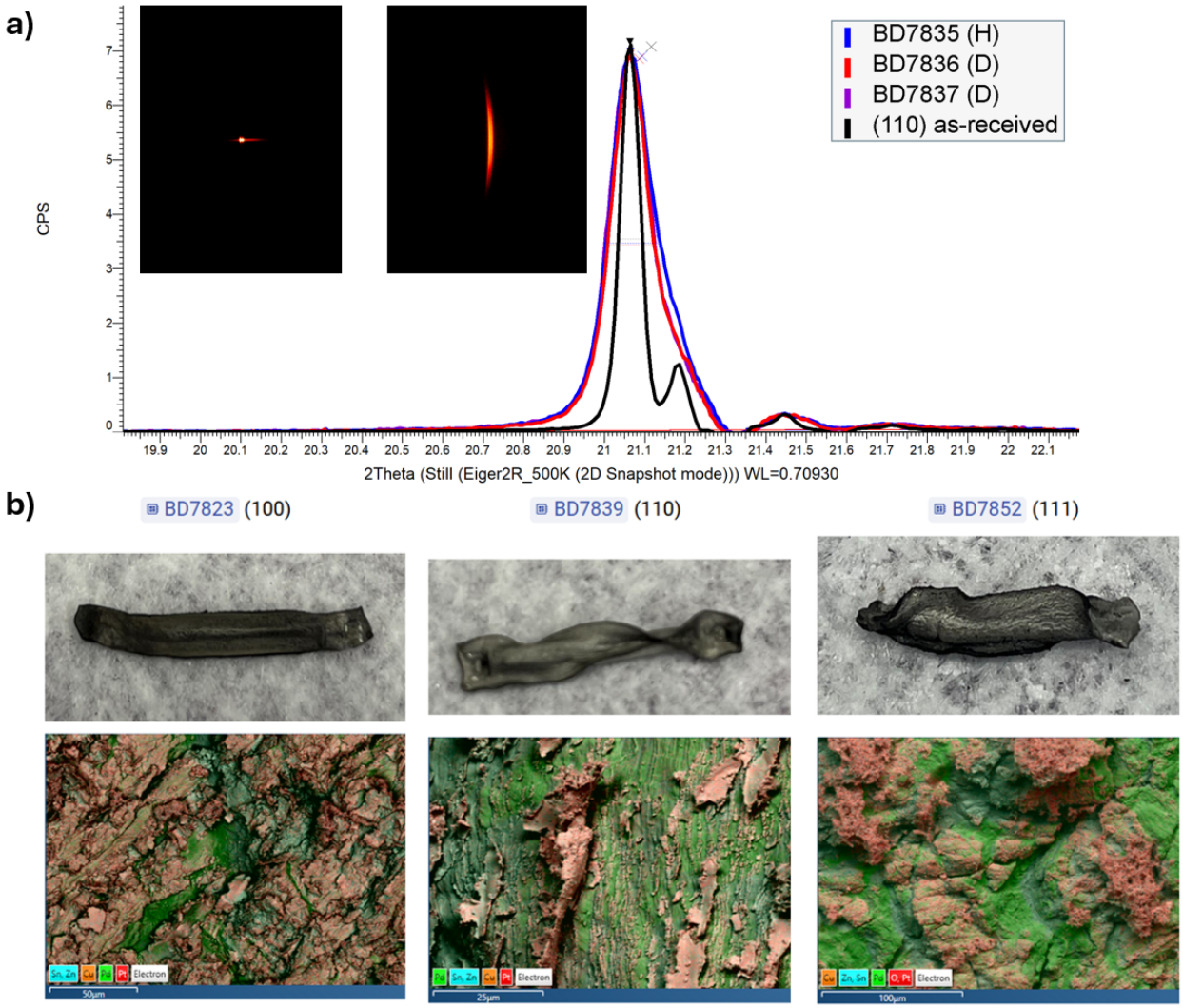

Fig. 8.10: a) Pre (left) and post (right) experimental XRD of the Pd (110) single crystal (BE3883). The diffractogram shows the peak broadening of the Pd single crystal after electrochemical loading (blue, red, and purple) compared to its original state (black). b) Shows the sample deformation that occurs after AC cycling (BE4182) for each crystal orientation (100), (110), and (111) respectively. Samples are 3 mm x 29 mm. Below each image is an EDS false color map scan showing the presence of coating-x and its typical elements (i.e., Zn, Cu, and Pt).

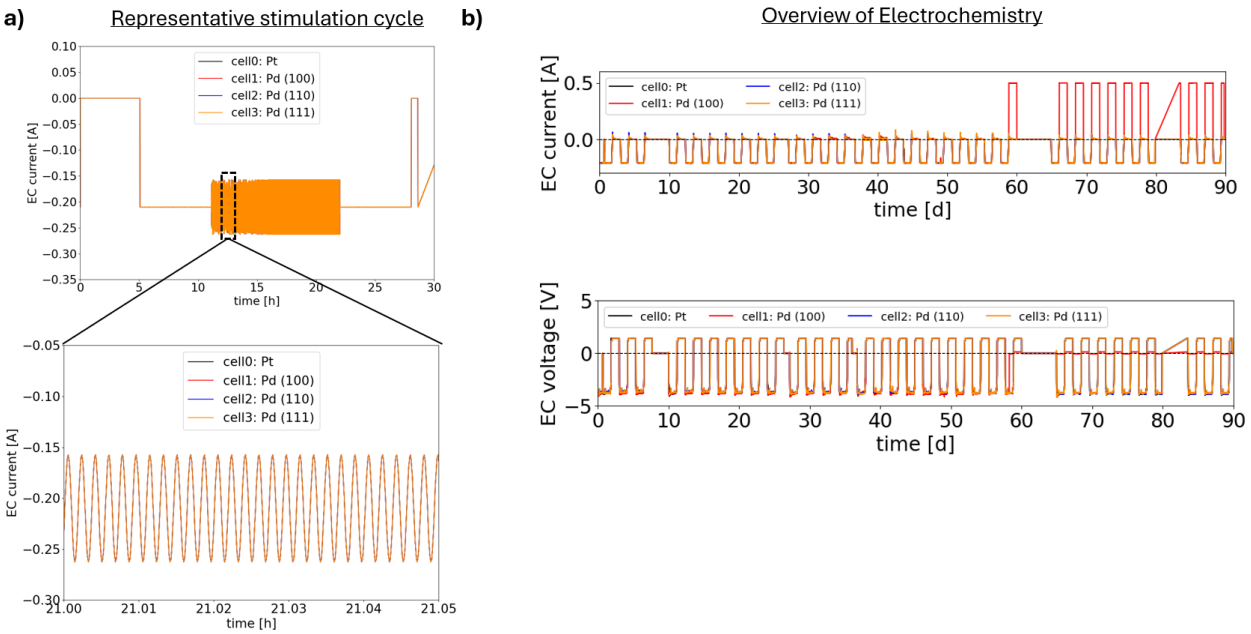

Fig. 8.11: a) Representative example of the AC EC stimulation applied to the Pd single crystal samples where current was alternated between -0.25 A to -0.15 A with an average current of -0.20 A. b) Overview of the current and voltage application (36 cycles) for the Pd single crystal samples (BE4182).

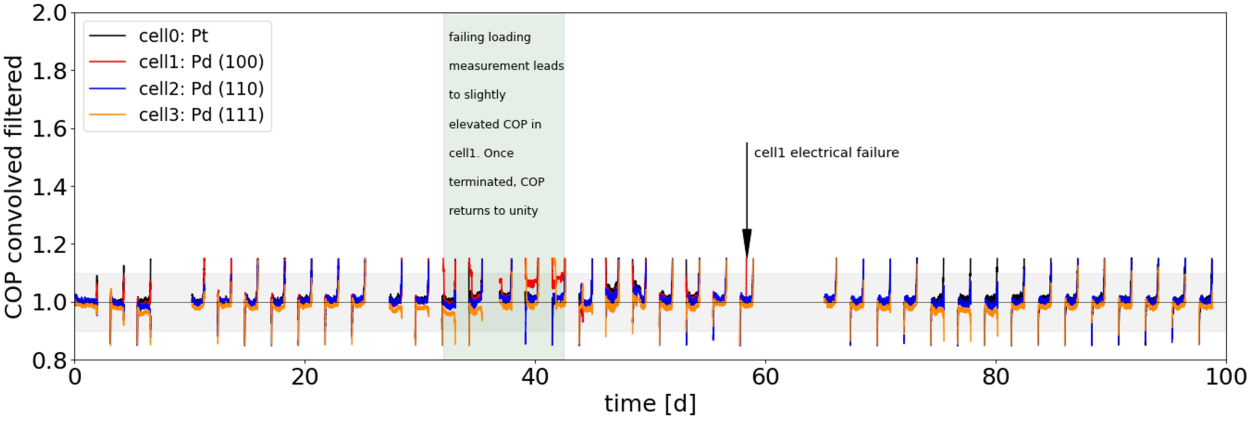

Fig. 8.12: Overview of the Pd (100), (110), and (111) single crystals AC EC stimulation (BE4182). Transients in signal are due changes in input power. The region highlighted in green is where a failed loading measurement led to a slightly elevated COP in cell 1.

8.4 Alloys

When palladium alloys with other metals, its material characteristics can change significantly. These changes can affect mechanical, electronic, and optical properties – often a combination of these. Fundamentally, these alterations arise from the way different alloying elements modify bonding within the crystal lattice. One key aspect is atomic size effects: elements with atomic radii different from palladium can introduce atomic strain into the alloy. This strain can impact both the mechanical strength and the electronic structure of the material, influencing properties such as ductility and hardness. For instance, alloying palladium with larger atoms may induce lattice distortions, increasing stress and possibly affecting hydrogen diffusion and absorption [295, 296]. In addition to size effects, the electronic structure of the alloying element plays a crucial role. When elements with different electron configurations are introduced into the palladium lattice, they can alter the electronic density and band structure. This can shift palladium's catalytic properties and hydrogen solubility, affecting how hydrogen isotopes enter and interact with the lattice [295, 296].

These electronic and structural changes can also impact the electrocatalytic properties of the alloy, especially in reactions like water splitting. The kinetics of the Volmer, Tafel, and Heyrovsky steps in hydrogen evolution reactions (HER) can differ between pure palladium and its alloys. For example, larger alloying elements could reduce the energy barrier for hydrogen recombination, leading to slower Tafel kinetics, while simultaneously allowing for higher hydrogen loadings. Conversely, other alloys may reduce deuterium loading. Ultimately, our interest in alloys was pragmatic. It wasn't that we were attached to palladium per se, but any material that could produce excess heat was of value. Given the materials explored in the literature and the reports of excess heat in palladium systems, we reasoned that alloying palladium could minimize the risks in our experimental exploration, especially considering the resources, instrumentation, and time constraints. With this in mind, we explored several alloy systems, including PdAg (palladium-silver), PdRh (palladium-rhodium), PdNi (palladium-nickel), and what we termed complex palladium alloys. The PdAg system, for example, is well known for its improved hydrogen absorption kinetics and mechanical properties compared to pure palladium. PdRh alloys, on the other hand, are valued for their enhanced stability and resistance to hydrogen embrittlement, which makes them suitable for long-term hydrogen cycling.

Our most ambitious effort was in the category of complex palladium alloys, where we synthesized two distinct alloys containing palladium and 12 different elements, each at around 1% by weight. These elements were chosen based on their natural occurrence in palladium ores, representing the most common impurities introduced from the mining-to-manufacturing process. This approach aligns with recent interest in high-entropy alloys (HEAs) - materials composed of multiple principal elements that potentially exhibit novel and often superior properties, such as improved mechanical strength, corrosion resistance, and enhanced hydrogen storage [297]. Although we cannot conclusively verify the uniqueness of our complex palladium alloys, based on a thorough review of the literature, they appear to be relatively unexplored. We subjected these alloys to different types of electrochemical stimulation (typically -50 mA of DC current with alternating loading/deloading cycles), but ultimately did not observe any excess heat. Here is an overview of the experiments: PdRh (Figure 8.13), PdAg (Figure 8.14), and PdNi (Figure 8.15) wires were all subjected to electrochemical conditions described previously in the HTCal system. No excess heat was observed in any of these sample compositons. Ni cathodes were also subjected to typical electrochemical conditions in the HTCal system. Additionally, we explored depositing thin films of palladium onto Ni cathodes in order to try and increase deuterium loading into the nickel lattice. We did not observe any resistance changes other than what was expected from temperature changes. This contradicts claims in the literature that pure nickel cathodes uptake hydrogen isotopes under ambient electrochemical conditions [298]. In these tests, no excess heat was observed. An example of overview data is shown in Figure 8.16.

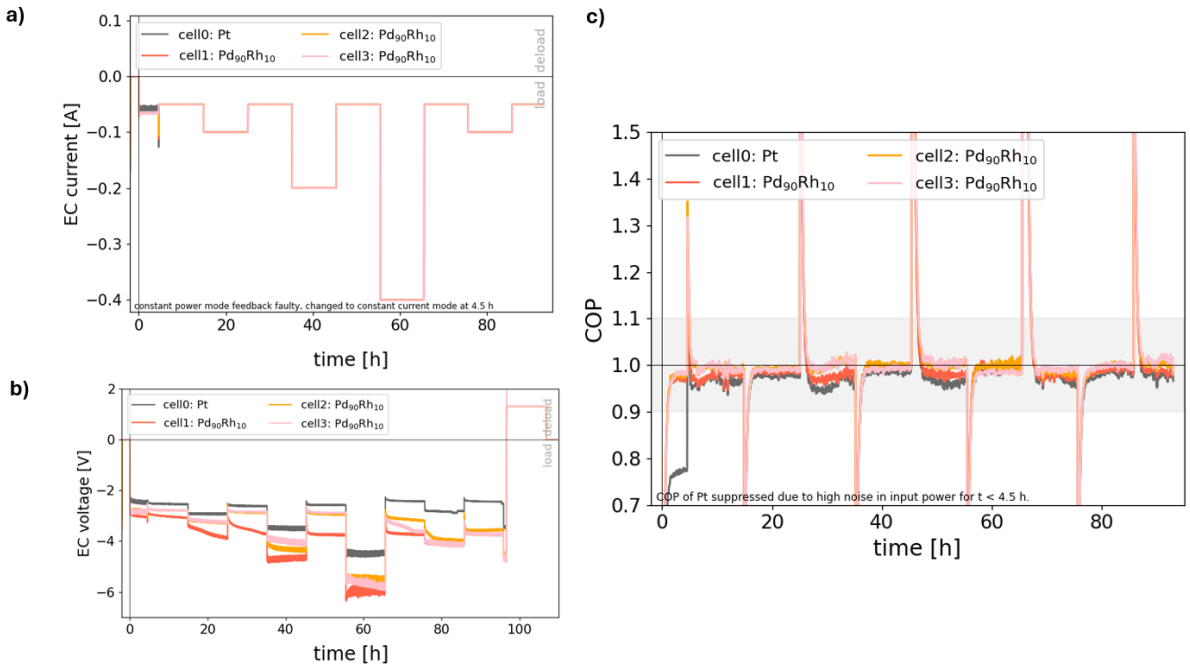

Fig. 8.13: Summary figure of the $Pd_{90}Rh_{10}$ alloy sample with a) current, b) voltage, and c) COP data. Transients are due to changes in input power.

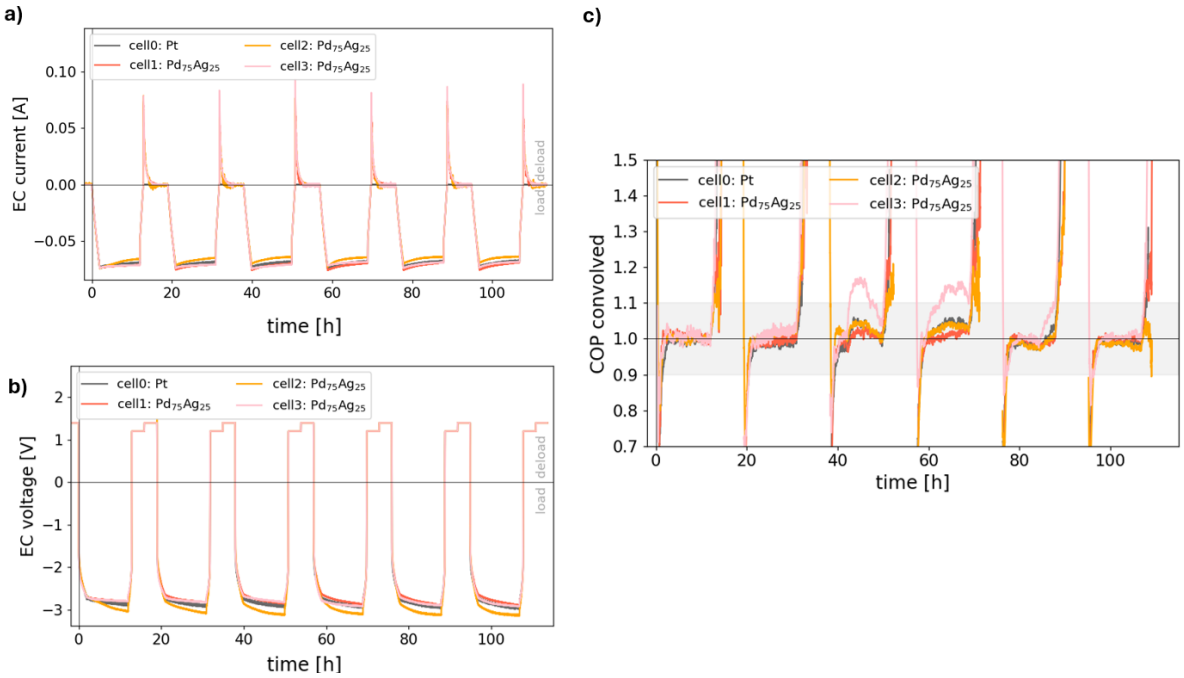

Fig. 8.14: Summary of the $Pd_{75}Ag_{25}$ alloy sample with a) current, b) voltage, and c) COP data. Transients are due to changes in input power.

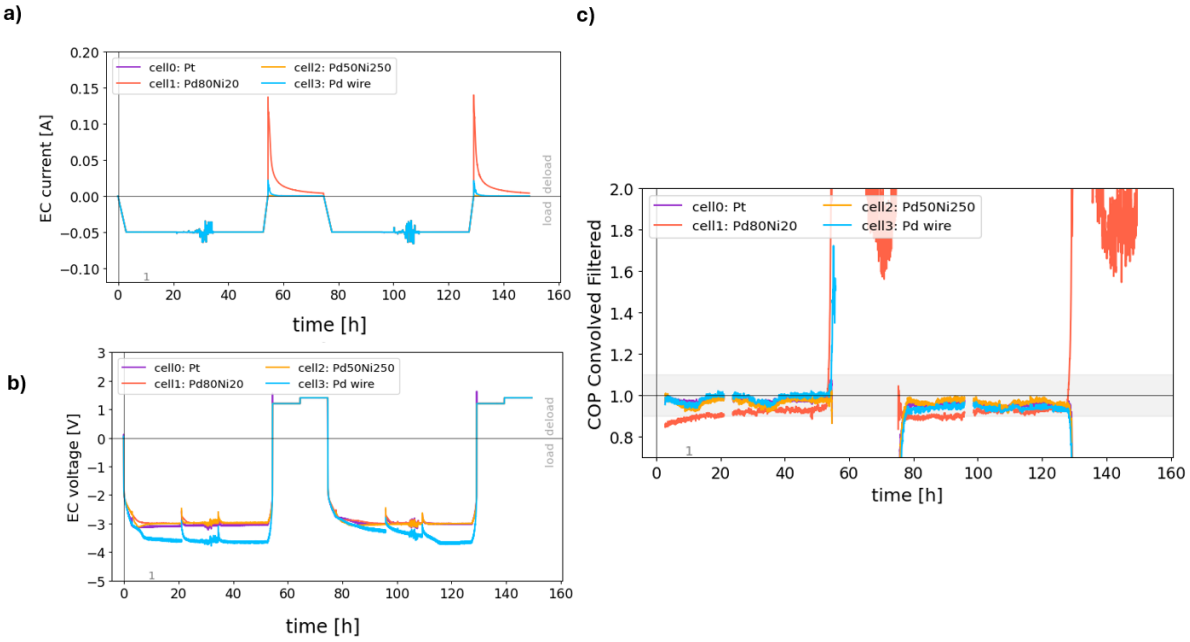

Fig. 8.15: Summary of the $Pd_{80}Ni_{20}$ alloy sample with a) current, b) voltage, and c) COP data. Transients are due to changes in input power, and noise in the COP of $Pd_{80}Ni_{20}$ (red) sample during deload is an artificial reading due to recombination during deloading.

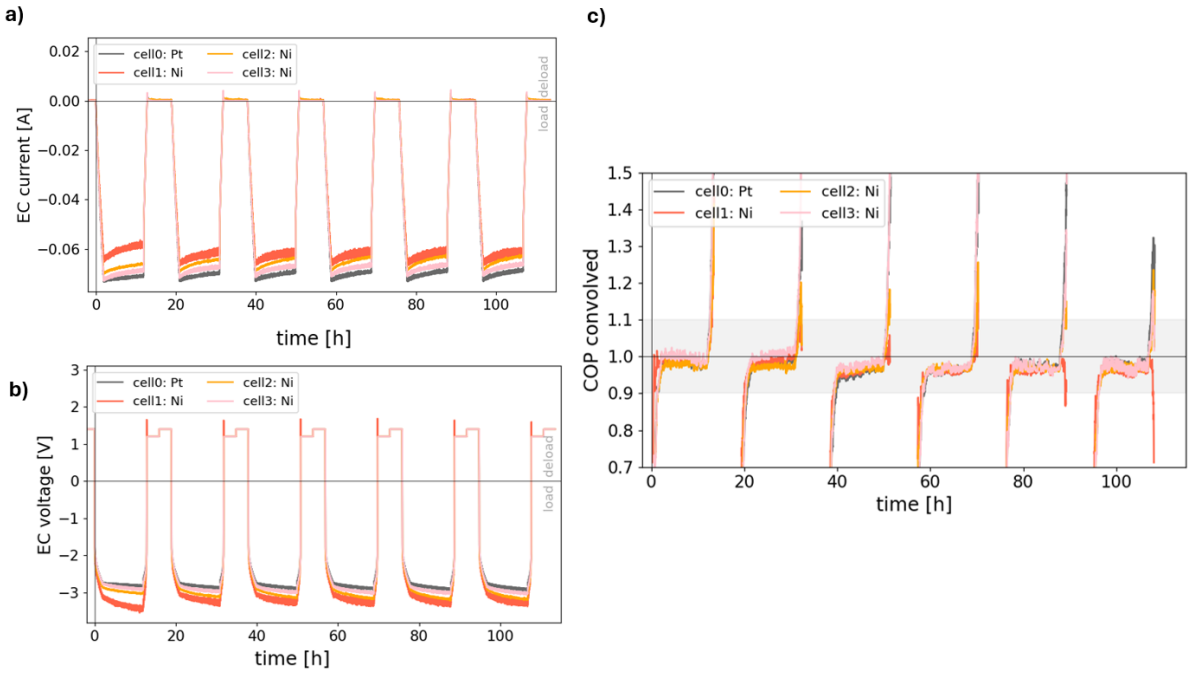

Fig. 8.16: Summary of the Ni cathode sample with a) current, b) voltage, and c) COP data. Transients are due to changes in input power.

We wanted to explore a wider range of impurities found in Pd alloys in an efficient amount of time. In order to address this, we worked with Goodfellow to manufacture custom, complex Pd alloys with 12 different alloyed elements, as previously described. Complex 1's composition is (Pd (88%), Si (1%), S (1%), Fe (1%), Zn (1%), Ge (1%), Se (1%), Ag (1%), In (1%), Sb (1%), Te (1%), Pb (1%), Bi (1%)) and Complex 2's composition is (Pd (88%), Fe (1%), Ni (1%), Cu (1%), Zn (1%), Ge (1%), Se (1%), In (1%), Sn (1%), Sb (1%), Te (1%), Pb (1%), Bi (1%)). Upon receiving the complex alloys, we performed x-ray diffraction to ensure that the cathode was still a single-phase material. Despite the incredible compositional complexity of these materials, at 1 wt% of each element present, we were able to confirm them as single phase materials – to the detection limits of our x-ray diffraction technique, which is around 0.1 % by volume. We subjected these materials to long duration electrochemical stimulation (>65 days of DC current held at 200 mA after three pre-cycles), however, we only observed false heat signals. These false signals arose from transient recombination, failed electrical contacts, and network errors that resulted in the loss of data for brief periods of time. Given the several month long duration of these tests which pushed the limit of the HTCal without any servicing or repair, these failure modes were not entirely unexpected. Examples of the data from these tests are shown in Figure 8.17.

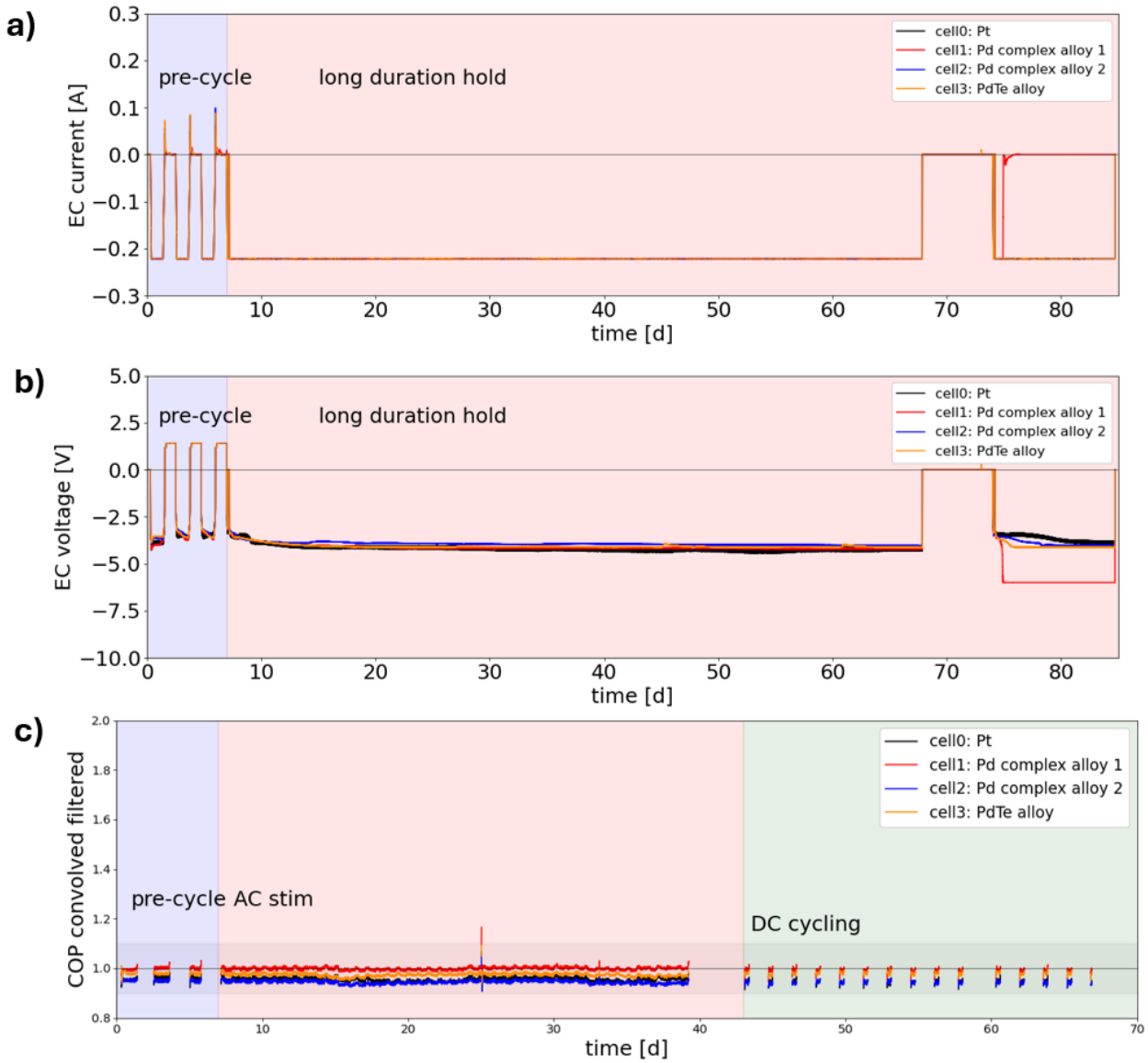

Fig. 8.17: Summary of the two experiments carried out with complex alloy samples a) current and b) voltage for the long duration EC hold (BE4309), and c) COP data of the AC stimulation and DC cycling experiment (BE4308). Pre-cycle highlighted in blue, AC stim cycle is in red, and the DC cycle is in green. Transients are due to changes in input power.